

Mobile authentication of copy detection patterns

Olga Taran, Joakim Tutt, Taras Holotyak, *Member, IEEE*, Roman Chaban, Slavi Boney, Slava Voloshynovskiy, *Senior Member, IEEE*

Department of Computer Science, University of Geneva, Switzerland
 {olga.taran, joakim.tutt, taras.holotyak, roman.chaban, slavi.boney, svolos}@unige.ch

Abstract—In the recent years, the copy detection patterns (CDP) attracted a lot of attention as a link between the physical and digital worlds, which is of great interest for the internet of things and brand protection applications. However, the security of CDP in terms of their reproducibility by unauthorized parties or clonability remains largely unexplored. In this respect this paper addresses a problem of anti-counterfeiting of physical objects and aims at investigating the authentication aspects and the resistances to illegal copying of the modern CDP from machine learning perspectives. A special attention is paid to a reliable authentication under the real life verification conditions when the codes are printed on an industrial printer and enrolled via modern mobile phones under regular light conditions. The theoretical and empirical investigation of authentication aspects of CDP is performed with respect to four types of copy fakes from the point of view of (i) multi-class supervised classification as a baseline approach and (ii) one-class classification as a real-life application case. The obtained results show that the modern machine-learning approaches and the technical capacities of modern mobile phones allow to reliably authenticate CDP on end-user mobile phones under the considered classes of fakes¹.

Index Terms—Authentication, copy detection patterns, copy fakes, multi-class classification, one-class classification.

I. INTRODUCTION

IN the modern world of globally distributed economy it is extremely challenging to ensure a proper production, shipment, trade distribution, consumption and recycling of various products and goods of physical world. These products and goods range from everyday food to some luxury objects and art. Creation of digital twins of these objects with appropriate track and trace infrastructures complemented by cryptographic tools like blockchain represents an attractive option. However, it is very important to provide a robust, secure and unclonable link between a physical object and its digital representation in centralized or distributed databases. This link might be implemented via overt channels, like personalized codes reproduced on products either directly or in a form of coded symbologies like 1D and 2D codes or covert channels, like invisible digital watermarks embedded in images or text or printed by special invisible inks. However, many codes of this group are easily copied or can be regenerated. Thus, there is a great need in unclonable modalities that can be easily integrated with the printable codes. This necessity triggered

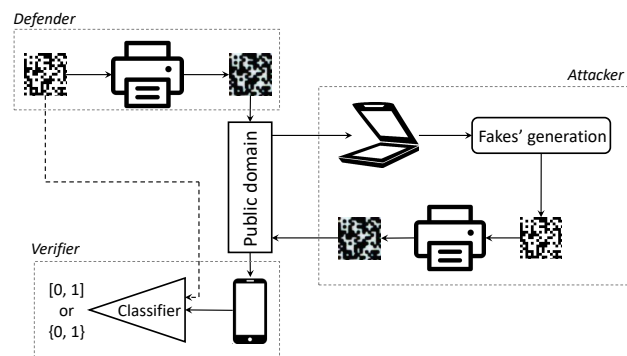


Fig. 1: General scheme of the CDP life cycle: (i) the generated digital templates are printed by a defender and go to the public domain; (ii) an attacker having an access to the publicly available printed codes can produce different type of fakes that are then also distributed in the public domain; (iii) a verifier digitizes the printed codes from the public domain and validates them via a classifier that might produce either a hard decision (fake/authentic) $\sim 0/1$ or kind of a soft decision ranging from 0 to 1. The validation might be produced with or without taking the digital templates into account. For the defender-verifier pair the protection problem consists in the minimization of probability of error as a function of the CDP design, used printing and acquisition technologies, type of attacks if such is known and used classifier. For the attacker the goal is to maximize the probability of error as a function of the attack construction.

the appearance and growing popularity of Printable Graphical Codes (PGC). During the last decade, the PGC attracted many industrial players and governmental organizations. One of the most popular nowadays type of PGC is a union of traditional 2D codes and *copy detection patterns* (CDP) [1].

General scheme of the CDP life cycle is shown in Fig. 1. The CDP security is based on a so-called information loss principle: each time the code is printed or scanned some information about the original digital template is inevitably lost. In the case of printable codes, the information loss principle is based on physical phenomena of random interaction between the ink or toner with a substrate. As a result any dot undergoes a complex unpredictable modification and changes its shape accordingly to a dot gain effect. Generally, the black dot increases in its size. A white hole on a black background accordingly decreases its area due to the dot gain of nearest black dot surround.

S. Voloshynovskiy is a corresponding author.

This research was partially funded by the Swiss National Science Foundation SNF No. 200021_182063.

¹The partial results from this work were submitted to the special session on "Forensics and Security of Physical Objects" of the IEEE International Workshop on Information Forensics and Security 2021.

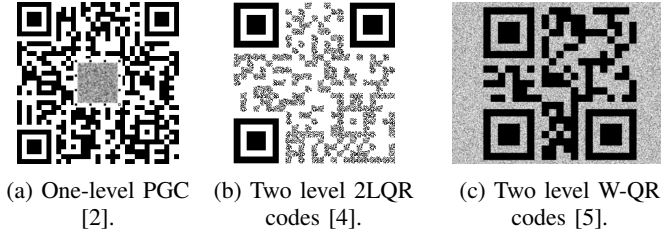


Fig. 2: Examples of different types of modern PGC with CDP modulations.

In the case of image acquisition the information loss principle refers to a loss of image quality due to various factors that include variability of illumination, finite and discrete nature of sampling in CCD/CMOS sensors, non-linearity in sensor sensitivity, sensor noise and various sensor defects, etc. All together, the enrolled image is characterized by some variability that degrades the quality of image in terms of its correspondence to the original digital template from which the code was printed.

Nowadays, there exists a big variety of different approaches aiming to combine CDP and widely used traditional 2D codes. Without pretending to be exhaustive in the presented overview, some of the most representative approaches are mentioned below.

In general, it is possible to distinguish the standard one-level PGC and more advanced multi-level PGC. Examples of these codes are given in Fig. 2. The one-level PGC is shown in Fig. 2a. According to the presented design, a CDP central part is inserted into a structure of 2D QR-code [2]. Originally the multi-level PGC aimed at increasing the storage capacity of the regular PGC [3]. Recently, the multi-level PGC are considered as a tool to increase the security of standard PGC. Without loss of generality, it is possible to identify the multi-level PGC with a modulation of the main black symbols as shown in Fig. 2b and a background modulation as illustrated in Fig. 2c.

The most well known multi-level PGC of the first type are so-called two level QR (2LQR) codes proposed in [6], [4], where the standard black modules are substituted by special modulated patterns. The general principles of modulation of multi-level codes were initially considered and theoretically analysed in [7]. The public level of this code is read as normal standard QR code. The texture patterns are chosen to be sensitive to the print & scan process. At the same time, the modulation pattern can carry out private message. Furthermore, the idea of 2LQR was extended in [8] by the use of different encrypting strategies. The anti-counterfeiting performance of these codes was mainly tested based on desktop printers and scanners [6], [4]. Thus, there is a great interest in validation of these codes under the industrial printing and mobile phone authentication.

The second type of multi-level PGC is so-called W-QR codes proposed in [5], where the authors substitute the background of a standard QR code by a specific random texture. The embedded texture does not affect the readability of the standard code but it should be sensitive to the print & scan

process in such a way to give a possibility to authenticate the original code from the counterpart. The authors propose a particular random textured pattern, which has a stable statistical behavior. Thus, the attacker targets to estimate the parameters of the used textured pattern.

Despite the differences in ways how the traditional QR codes and CDP are combined, in general case, the authentication of digital artwork based on the CDP is done by comparing the reference template with the printed version scanned using a scanner or camera of mobile phone. As a reference template there can be used either a digital template or enrolled printed version of the same artwork. The comparison can be done in different ways either in the spatial or frequency domain using a correlation, distance metrics or a combined score of different features, etc., [1], [9]. Alternatively, one can also envision an authentication in a transform domain using latent space of pretrained classifiers or auto-encoders [10].

Despite a great interest, the robustness of CDP, used in PGC, to the copy attacks remains a little studied problem. Therefore, the current work is dedicated to the investigation of the authentication aspects of CDP under industrial settings from the perspective of modern machine learning.

The main contributions of this paper are:

- We created an Indigo mobile dataset of CDP printed on the industrial printer HP Indigo 5500 DS under the regular industrial settings to make the research conditions as close as possible to the real-life situations. The printed codes were enrolled via mobile phone iPhone XS under the regular light conditions.
- We investigated the multi-class supervised classification of CDP from the information-theoretic point of view and study the role of different types of fakes on the authentication accuracy of supervised classifier.
- We investigated the authentication aspects of the CDP from the perspective of one-class classification in the spatial and deep processing domains.
- For the one-class classification in the deep processing domain we investigated the feature extractor model based on the auto-encoding principle that we studied from the information-theoretic point of view.

Notations: We use the following notations: $\mathbf{t} \in \{0, 1\}^{m \times m}$ denotes an original digital template; $\mathbf{x} \in \mathbb{R}^{m \times m}$ corresponds to an original printed code, while $\mathbf{f} \in \mathbb{R}^{m \times m}$ is used to denote a printed fake code; $\mathbf{y} \in \mathbb{R}^{m \times m}$ stands for a probe that might be either original or fake. $p_t(\mathbf{t})$ and $p_{\mathcal{D}}(\mathbf{x})$ correspond to empirical data distributions of the digital templates and original printed codes, respectively. The discriminators corresponding to Kullback–Leibler divergences are denoted as \mathcal{D}_x , where the subscript indicates the space to which this discriminator is applied to.

II. DATASETS

A. State-of-the-art datasets

The majority of the research experiments in the domain of CDP are performed either on synthetic data or on small private datasets. The production of datasets of real CDP is a very time consuming and quite costly process. It requires the

TABLE I: An overview of the datasets of CDP: the datasets (1) and (2) are publicly available state-of-the-art datasets and the dataset (3) is created and investigated in the current paper.

Name	Digital templates	Printing	Acquisition	# of codes
(1) DPIC & DP1E [10]	size: 384×384 symbol size: 6×6	<i>Laser</i> , at 1200 dpi: • Samsung Xpress 430 • Lexmark CS310 <i>Inkjet</i> , at 1200 dpi: • Canon PIXMA iP7200 • HP OfficeJet Pro 8210	<i>Scanner</i> : • Canon 9000F at 1200 ppi • Epson V850 Pro at 1200 ppi	digital: 384 original: 3072 fakes: 3072 total: 6528
(2) CSGC [11]	size: 100×100 symbol size: 1×1	<i>Laser</i> , at 600 dpi: • Xerox Phaser 6500	<i>Scanner</i> : • Epson V850 Pro at 2400 ppi at 4800 ppi at 9600 ppi	digital: 950 original: 2850 total: 3800
(3) Indigo mobile	size: 330×330 symbol size: 5×5	<i>Industrial</i> , at 812 dpi: • HP Indigo 5500 DS	<i>Mobile phone</i> : • iPhone XS auto settings	digital: 300 original: 300 fakes: 1200 total: 1800



(a) Binary digital template. (b) Printed original code.

Fig. 3: Examples of (a) a binary digital template used for printing and (b) the printed original code from the Indigo mobile dataset enrolled by the mobile phone.

printing and acquisition of the original CDP, the production and acquisition of fakes preferably on the equipment close to the industrial one.

Up to our best knowledge, there are only few publicly available datasets summarized in Table I that were created to investigate the clonability aspects of CDP:

- (1) The DP0E [12] and its extension DP1E & DP1C [10] are the datasets of real and counterfeited CDP based on *DataMatrix* modulation [13] produced with four printers and enrolled by the high resolution scanners. The DP1E & DP1C dataset contains 6528 codes produced from 384 digital templates with symbol size 6×6 elements, with 3072 printed original codes and 3072 fake codes printed on the same printers as original codes.
- (2) The CSGC dataset [11] consists of 3800 codes produced from 950 digital templates with symbol size 1×1 elements and 2850 original codes printed on the Xerox Phaser 6500 laser printed at 600 dpi and scanned by the Epson V850 Pro scanner under three different resolutions summarized in Table I.
- (3) In the current work in order to investigate the authentication aspect of the CDP under the real-life conditions, we created a new dataset: an Indigo mobile dataset of codes printed on the industrial printer HP Indigo 5500 DS (Table I). The main objective of this dataset is to investigate the general authentication capabilities of CDP. In this regard, to make the authentication conditions

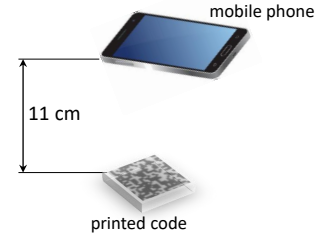


Fig. 4: The schematic representation of the mobile phone acquisition setup.

closer to the real life environment, instead of high quality scanners the printed codes are enrolled by using a mobile phone *iPhone XS* under regular room light conditions.

B. Indigo mobile dataset

Indigo mobile dataset includes 300 distinct digital *DataMatrix* templates $\mathbf{t} \in \{0, 1\}^{330 \times 330}$ with the symbols of size 5×5 elements². An example of the digital template is given in Fig. 3a. The digital templates consist of the central CDP and four synchro-markers that allow to make an accurate synchronization and cropping of the code of interest. To simulate the real life scenario, the generated digital templates were printed on the industrial printer *HP Indigo 5500 DS* at the resolution 812 dpi³. The acquisition of the printed codes is performed under regular room light using mobile phone *iPhone XS* (12 Mpixels) under the automatic photo shooting settings in Lightroom application⁴. The mobile phone is held parallel to the printed code at height 11 cm as schematically

²To ensure accurate symbol representation, each printed symbol should be represented by at least 3×3 pixels. Taking into account the difference between the industrial printing resolution (about 812 dpi) and the average resolution of the mobile phones (about 600 - 900 ppi) especially in the development countries, where the problem of counterfeiting is particularly important, one can estimate the symbol size from about 4×4 till 5×5 pixels.

³It should be pointed out that the native printing resolution of HP Indigo 5500 DS is 812.8 dpi. The impact of printing resolution and the symbol size is a subject of our ongoing research.

⁴<https://apps.apple.com/us/app/adobe-lightroom-photo-editor/id878783582>

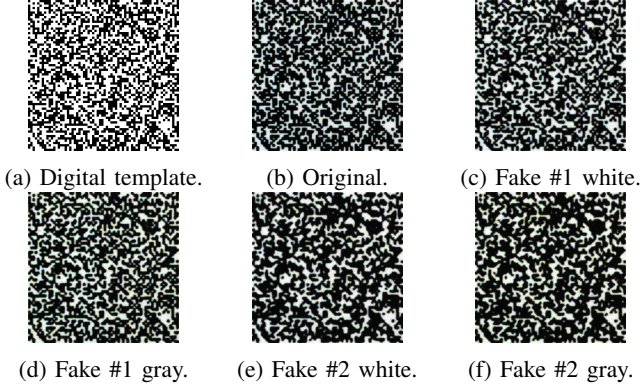


Fig. 5: Examples of original and fake codes with symbol size 5×5 elements taken by a mobile phone from the Indigo mobile dataset.

shown in Fig 4. The photos are taken in DNG format to avoid built-in mobile phone image post-processing. An example of obtained photo is shown in Fig. 3b. The following cropping of the code is performed in an automatic way by applying a geometrical synchronization with four squared synchronomarkers. Finally, the cropped codes are converted to the RGB format⁵. The obtained codes are $\mathbf{x} \in \mathbb{R}^{330 \times 330}$ with symbols' size 5×5 elements. Examples of the obtained code is shown in Fig. 5b.

To simulate typical scenario for an unexperienced counterfeiter, we produce copies based on standard copy machines. The two different copy machines in copy regime "text" are used: (1) RICOH MP C307 and (2) Samsung CLX-6220FX. The fakes are produced on two types of paper: white paper 80 g/m² and gray paper 80 g/m².

Thus, we produced four fake codes for each original printed code:

- 1) *Fakes #1 white*: made by the copy machine (1) on the white paper.
- 2) *Fakes #1 gray*: made by the copy machine (1) on the gray paper.
- 3) *Fakes #2 white*: made by the copy machine (2) on the white paper.
- 4) *Fakes #2 gray*: made by the copy machine (2) on the gray paper.

To be coherent with the enrolled original printed codes, the acquisition of the produced fakes is performed in the same way using the same mobile phone under the same photo and light settings as for the original printed codes.

In total, the Indigo mobile dataset contains 1800 codes: 300 distinct digital templates; 300 enrolled original printed codes and 1200 enrolled fake printed codes: 300 originals \times 4 type of fakes⁶.

Examples of the obtained digital, original and fake codes are shown in Fig. 5. Due to a built-in morphological processing of the Ricoh copy machine the fakes #1 are more accurate

⁵https://docs.opencv.org/4.5.2/d8/d01/group_imgproc_color_conversions.html#ga397ae87e1288a81d2363b61574eb8cab

⁶The Indigo mobile dataset is available at <https://github.com/sip-group/snf-it-dis/tree/master/datasets/indigomobile>.

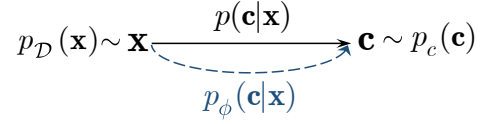


Fig. 6: Supervised classification problem: general formulation.

with a dot gain close to the original codes. In the case of the fakes #2 the dot gain is much higher and, as a result, the symbols contain more black ink and look darker. Visually the difference between the two types of used paper is not evident.

For the empirical evaluation the Indigo mobile dataset was split into three sub-sets: *training* with 40% of data, *validation* with 10% of data and 50% of data is used for the *test*. To avoid the bias in the choice of training and test data, each investigated model was trained five times under randomly splitting data between these subsets. Moreover, the following data augmentations were used: (i) the rotations on 90°, 180° and 270°; (ii) the gamma correction with variable function $(\cdot)^\gamma$, where $\gamma \in [0.5, 1.2]$ with step 0.1 is the parameter of gamma correction.

III. MULTI-CLASS SUPERVISED CLASSIFICATION

A. Theoretical analysis

The supervised multi-class classification is chosen as a baseline to validate the authentication efficiency of CDP. The complete availability of fakes at the training stage for the classification gives the defender an information advantage over the attacker. Such a scenario is an ideal case for the defender and the worst case for the attacker. It assumes that, besides the original digital templates $\{\mathbf{t}_i\}_{i=1}^M$ and the corresponding printed codes $\{\mathbf{x}_i\}_{i=1}^M$, the defender has an access to the fake codes $\{\mathbf{f}_i\}_{i=1}^{M_f}$, $M_f \leq M$.

From the information-theoretic point of view the problem of a supervised classifier training given the labeled data $\{\mathbf{x}_i, \mathbf{c}_i\}_{i=1}^N$ generated from a joint distribution $p(\mathbf{x}, \mathbf{c})$ is formulated as a training of a parameterized network $p_\phi(\mathbf{c}|\mathbf{x})$ that is an approximation of $p(\mathbf{c}|\mathbf{x})$ originating from the chain rule decomposition $p(\mathbf{x}, \mathbf{c}) = p_{\mathcal{D}}(\mathbf{x})p(\mathbf{c}|\mathbf{x})$. The training of the network $p_\phi(\mathbf{c}|\mathbf{x})$ is performed based on the maximisation of a mutual information $I_\phi(\mathbf{X}; \mathbf{C})$ between \mathbf{x} and \mathbf{c} via $p_\phi(\mathbf{c}|\mathbf{x})$:

$$\hat{\phi} = \underset{\phi}{\operatorname{argmax}} I_\phi(\mathbf{X}; \mathbf{C}), \quad (1)$$

that can be rewritten as:

$$\hat{\phi} = \underset{\phi}{\operatorname{argmin}} \mathcal{L}_{\text{Supervised}}(\phi), \quad (2)$$

where $\mathcal{L}_{\text{Supervised}}(\phi) = -I_\phi(\mathbf{X}; \mathbf{C})$.

The mutual information in (1) is defined as:

$$\begin{aligned} I_\phi(\mathbf{X}; \mathbf{C}) &\triangleq \mathbb{E}_{p(\mathbf{x}, \mathbf{c})} \left[\log \frac{p_\phi(\mathbf{c}|\mathbf{x})}{p_c(\mathbf{c})} \right] \\ &= \underbrace{\mathbb{E}_{p(\mathbf{x}, \mathbf{c})} [\log p_\phi(\mathbf{c}|\mathbf{x})]}_{\mathcal{D}_{c|\mathbf{x}}} - \underbrace{\mathbb{E}_{p_c(\mathbf{c})} [\log p_c(\mathbf{c})]}_{=\text{constant}}, \end{aligned} \quad (3)$$

where $H(\mathbf{C}) = -\mathbb{E}_{p_c(\mathbf{c})} [\log p_c(\mathbf{c})]$ is the entropy of \mathbf{c} and it is a constant that does not depend on ϕ .

TABLE II: The classification error of the supervised multi-class classifier (in %).

Classification type	Originals	Fakes #1 white	Fakes #1 gray	Fakes #2 white	Fakes # 2 gray
2-class ^a	0.00	0.28 (± 0.3)			
3-class	0.00	0.78 (± 0.68)		0.35 (± 0.5)	
5-class	0.00	23.26 (± 7.55)	21.56 (± 0.81)	16.88 (± 6.62)	11.35 (± 4.89)

^a P_e corresponds to the P_{miss} for the originals and to the P_{fa} for the fakes.

Therefore, the optimisation problem (4) reduces to:

$$\hat{\phi} = \underset{\phi}{\operatorname{argmin}} \mathcal{L}_{\text{Supervised}}(\phi) = \underset{\phi}{\operatorname{argmin}} -\mathcal{D}_{cc}. \quad (4)$$

Remark: In practice the \mathcal{D}_{cc} term is optimized with respect to the cross-entropy loss.

B. Experimental results

The performance of the presented model (4) was empirically evaluated on the Indigo mobile dataset. The supervised multi-class classification is performed in two scenarios: (1) multi-class classification and (2) binary classification.

1) *Multi-class classification:* The multi-class supervised classification aims at investigating the performance of the base-line supervised classification scenario, where the model is trained on all classes of the data. Therefore, it corresponds to the case of the informed defender who knows all types of fakes in advance. At the inference stage, three validation scenarios are evaluated:

- 5-class classification: the ability of the model to distinguish all classes of the data, i.e., originals and four types of fakes.
- 3-class classification: the ability of the model to distinguish the originals, fakes from the first (fakes #1) and the second (fakes #2) groups.
- 2-class classification: the ability of the model to distinguish the originals from all types of fakes considered as a joint class.

Due to the relatively small amount of the codes in the Indigo mobile dataset and to avoid the bias in the selection of data for training and testing, the classification model is trained five times on the randomly chosen subset of data.

At the inference stage, the query sample \mathbf{y} , which might be either the original code \mathbf{x} or one of the fakes \mathbf{f}^k , $k = 1, \dots, 4$, is passed through a deterministic classifier g_ϕ such that $p_\phi(\mathbf{c}|\mathbf{x}) = \delta(\mathbf{c} - g_\phi(\mathbf{x}))$ and $\delta(\cdot)$ denotes the Dirac delta-function or simply $\mathbf{c} = g_\phi(\mathbf{x})$. Each class is encoded as one-hot-encoding with the class i^{th} represented as $\mathbf{c}_i = [0, \dots, 1, \dots, 0]^T$, with "1" in the position of i^{th} . Herewith, g_ϕ is trained with respect to the term \mathcal{D}_{cc} in (4). The term \mathcal{D}_{cc} represents the cross-entropy in this case. The obtained classification error $P_e = Pr[\hat{\mathbf{c}} \neq \mathbf{C} | \mathbf{C} = \mathbf{c}]$ is given in Table II. It is easy to see that the investigated model is capable to authenticate the original codes without mistakes in all considered scenarios.

The classification error about 0.28% in the two classes validation setup ("2-class" label in Table II) indicates that despite the visual similarity the classifier is capable to distinguish

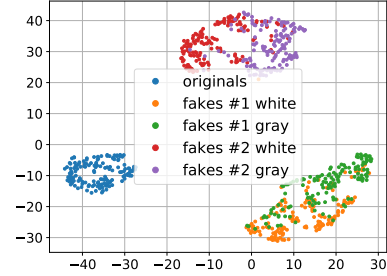


Fig. 7: T-SNE of the latent space (the last layer before an activation function) of the supervised classifier trained on originals and all type of fakes.

original and fakes with high enough accuracy. From the three classes validation scenario ("3-class" label in Table II), one can notice that the model confuses more the fakes #1 than fakes #2. The last validation scenario ("5-class" label in Table II) shows that for both groups of fakes the most difficult is to distinguish between the white and gray paper type of fakes. In addition, in Fig. 7 the t-SNE visualization [14] of the latent space (the last layer before an activation function) of the classifier trained in 5-class classification scenario is illustrated. From that visualization one can easily see the same phenomena: three main classes (originals, fakes #1 and fakes #2) are well separated while the samples printed on the white and gray papers overlap. This indicates that the substrate identification is a difficult problem even for the supervised classifier under the considered imaging setup.

2) *Binary classification:* The supervised binary classification aims at investigating the influence of the fakes' type used for the training on the model efficiency at the inference stage. In this respect, the training is performed separately on each type of fakes. Similarly to the multi-class classification scenario, in each case, the model is trained five times on the randomly chosen subset of data to avoid the bias in the training data selection. The difference between the 2-class classification and the considered binary classification consists in the assumption about the fakes available at the training. The 2-class classification assumes that all types of fakes are available at the training stage whereas the binary classification assumes that only one type of fakes is available and the rest fakes are unknown. Obviously, the binary classification is more challenging and the results will highly depend on the type of fakes chosen for training. At the test stage all fakes are present for the classification.

The binary classification accuracy is evaluated with respect

TABLE III: The classification error of the supervised binary classifier (in %) ^a.

Setup	Originals (P_{miss})	Fakes #1 white (P_{fa})	Fakes #1 gray (P_{fa})	Fakes #2 white (P_{fa})	Fakes # 2 gray (P_{fa})
Fakes #1 white	0	0	0.14 (± 0.32)	0	0
Fakes #1 gray	0	0	0	0	0
Fakes #2 white	0	99.43 (± 0.32)	100	0	0
Fakes # 2 gray	0	99.29 (± 0.5)	99.86 (± 0.32)	0	0

^aPresented binary classification is close to the multi-class classification scenario with 2 classes considered in Section III-B1. The difference in the obtained results is related to the presence of all types of fakes during the training in case of multi-class setup and randomly chosen training data.

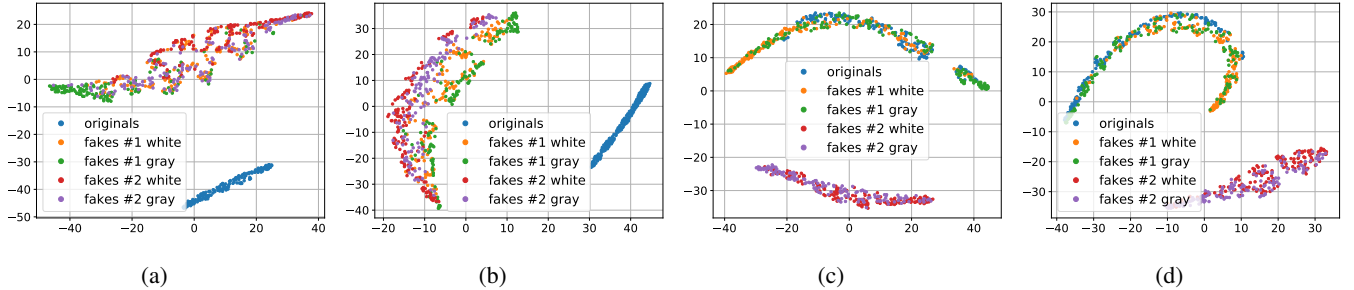


Fig. 8: The latent space (the last layer before an activation function) t-SNE visualization of the supervised binary classifier trained on the originals and (a) fakes #1 white, (b) fakes #1 gray, (c) fakes #2 white, (d) fakes #2 gray.

to the probability of miss P_{miss} and the probability of false acceptance P_{fa} defined as:

$$\begin{cases} P_{fa} &= \Pr\{g_{\phi}(\mathbf{Y}) = \mathbf{c}_1 \mid \mathcal{H}_0\}, \\ P_{miss} &= \Pr\{g_{\phi}(\mathbf{Y}) \neq \mathbf{c}_1 \mid \mathcal{H}_1\}, \end{cases} \quad (5)$$

where $\mathbf{c}_1 = [1, 0]^T$ denotes a class of original codes, \mathcal{H}_1 corresponds to the hypothesis that the query \mathbf{y} is an original code and \mathcal{H}_0 is the hypothesis that the query \mathbf{y} is a fake code.

From the obtained results presented in Table III one can note that both models trained on the originals and fakes #1 provide high classification accuracy on all type of data, including the fakes #2, unseen during the training. That is expected and can be explained by the fact that, as it is discussed in Section II-B, the fakes #1 are closer to the originals, while the fakes #2 are the coarser copies of the original codes. In this regard, when the training is performed on the fakes #2, no model is capable to distinguish the originals from the fakes #1, unseen during the training. That is confirmed by the probability of false acceptance close to 100%. Nevertheless, the models are capable to distinguish the originals from the fakes #2 with 100% accuracy. The t-SNE visualization of the latent space of each model illustrated in Fig. 8 confirms these observations. From Fig. 8a and 8b that present the latent space of models trained on the originals and the fakes #1, one can see the good separability between the originals and fakes while all classes of fakes overlap. The latent space visualization of models trained on the originals and fakes #2 illustrated in Fig. 8c and 8d shows the overlapping between the originals and the fakes #1 preserving the fakes #2 in well separable cluster.

IV. ONE-CLASS CLASSIFICATION

A. Spatial domain data analysis

In Section III it is shown that according to results obtained for the Indigo mobile dataset the original and fake codes are well separable in the latent space of the multi-class supervised classifier (Fig. 7). To answer the question how these data behave in the direct image domain (hereinafter also referred to as a *spatial domain*), the 2D t-SNE visualizations of the data in the spatial domain are shown in Fig. 9.

Fig. 9a shows the direct visualisation of the RGB images. One can note that the data do not form any clusters corresponding to originals or fakes. Instead, the data are allocated into small groups that are formed by the originals and fakes corresponding to the same digital template. Such a behavior is expectable and is explainable by the data nature.

Fig. 9b demonstrates a visualization based on the xor difference between the digital templates and the corresponding printed codes binarized via a simple thresholding method with an optimal threshold determined individually for each printed code via the Otsu's method [15]. In general, one can observe a kind of rings that consist of the original and fakes but no clusters specific to the data types are observed. These rings are explainable by the fact that both originals and fakes can have bigger or smaller difference with the digital template due to the dot gain in the different group of black and white symbols as shown in Fig. 10: a white symbol surrounded by the black symbols results in a bigger binarization error, while the black symbol surrounded by the white symbols is more likely to survive after binarization.

To better understand the role of the digital templates as a references, the Indigo mobile dataset was specially extended by the printed references (hereinafter also referred to as *physical*

TABLE IV: The OC-SVM classification error in spatial domain (in %) ^a.

Train on	Originals (P_{miss})	Fakes #1 white (P_{fa})	Fakes #1 gray (P_{fa})	Fakes #2 white (P_{fa})	Fakes #2 gray (P_{fa})
<i>With respect to the digital templates:</i>					
- grayscale \times	3.1 (± 0.83)	2.54 (± 1.93)	3.82 (± 1.22)	0	0
- RGB \times	2.82 (± 1.14)	2.1 (± 0.86)	1.4 (± 1.4)	0	0
<i>With respect to the physical references:</i>					
- grayscale \times	11.44 (± 4.14)	35.86 (± 7.38)	40.58 (± 4.86)	1.72 (± 2.07)	1.12 (± 0.8)
- RGB \times	11.16 (± 3.64)	31.84 (± 6.3)	39.54 (± 6.11)	1.44 (± 1.69)	0.98 (± 0.63)

^aThe python *OneClassSVM* method from the sklearn package is used with the next training parameters: kernel="rbf"; gamma=0.1; nu=0.03 for the digital templates and nu=0.1 for the physical references.

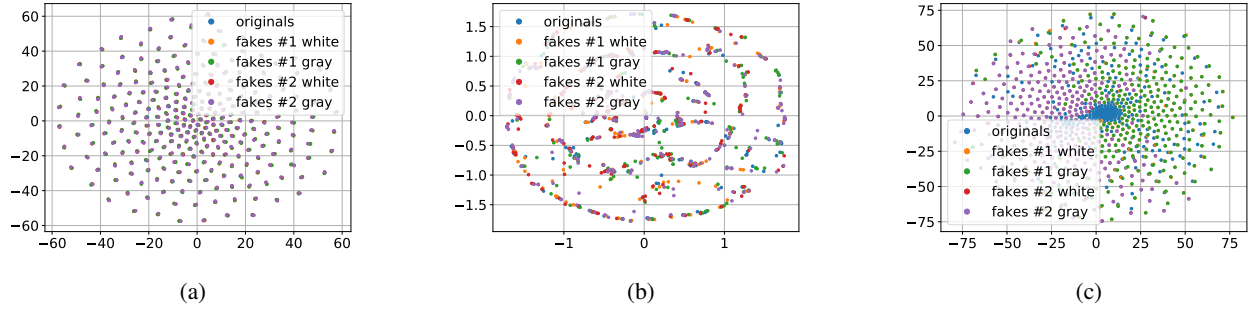


Fig. 9: The 2D t-SNE visualisation of the original and fake codes in the spatial domain (a horizontal axis denotes t-SNE dimension 1 and the t-SNE dimension 2 is on the vertical axis): (a) presents the direct RGB images' visualisation; (b) is based on the xor difference between the corresponding digital templates and printed codes binarized via a simple thresholding method with an optimal threshold determined individually for each printed code via the Otsu's method [15]; (c) visualizes the differences between the physical references and the corresponding printed original and fake codes.

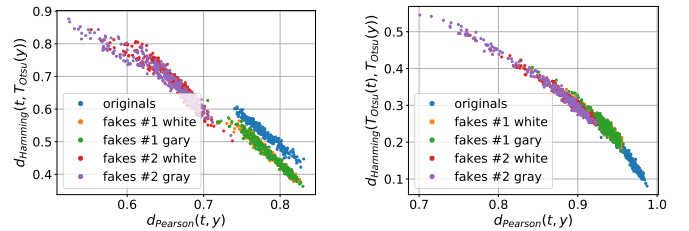


Fig. 10: Examples of the dot gain effect: (a) a black symbol surrounded by white symbols increases its size but remains well detectable; (b) a white symbol surrounded by black symbols might disappear under strong dot gain.

references⁷). It is easy to note the central dense cluster formed by the original codes (in blue) and two surrounding clusters from the fakes #1 (mostly on the right-hand side) and fakes #2 (mostly on the left-hand side) from Fig. 9c that illustrates the t-SNE of the differences between the physical reference and the corresponding printed original and fake codes. Despite this, the overall mixing of individual samples from the different classes is quite significant. This indicates that the reliable direct spatial authentication might be complicated.

As a next stage we performed the analysis of distances between the references (digital or physical) and the cor-

⁷The physical references correspond to the original codes acquired for the second time on the same equipment as the first case scenario. It assumes the probable presence of small geometrical (rotation) and illumination deviations between the original codes and corresponding physical references.



(a) With respect to the digital templates. (b) With respect to the physical references.

Fig. 11: The CDP separability in the 2D space of Pearson correlation (the horizontal axis) and Hamming distance (the vertical axis).

responding printed codes (original and fakes) in different metrics: ℓ_1 , ℓ_2 , Pearson correlation and Hamming distance. Whenever needed the binarization is applied via a simple thresholding with an optimal threshold determined individually for each code via the Otsu's method. The performed analysis demonstrates that besides some rare exceptions, it is impossible to separate the original and fake codes neither with respect to the digital template nor with respect to the physical reference based only on one metric. At the same time, the separability with respect to the two metrics is much better. The best two-metric separability we obtained is based on the Pearson correlation and Hamming distance between

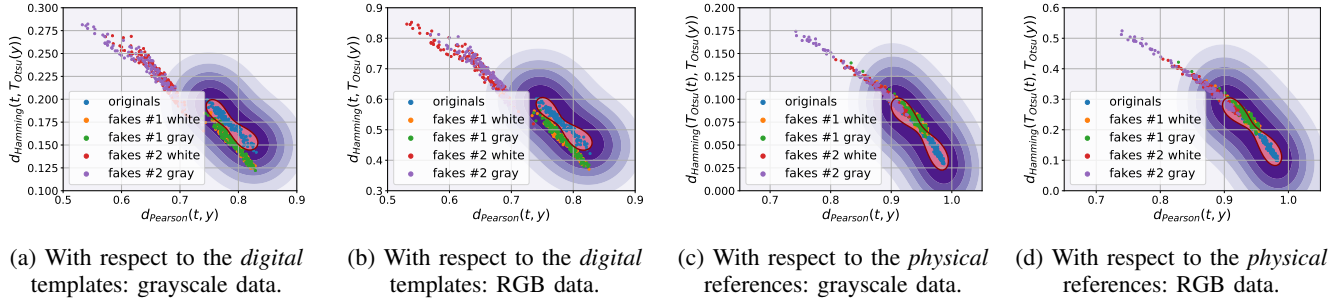


Fig. 12: The decision boundaries of OC-SVM trained with respect to the Pearson correlation and Hamming distance between the reference (digital or physical) and the corresponding original printed codes.

the printed codes and the corresponding digital or physical references as shown in Fig. 11a - 11b. Encouraged by these results we apply the one-class support vector machines (OC-SVM) [16] as a base-line approach for the classification of originals and fakes.

To better understand the role of used reference and the influence of color information during the acquisition of black and white codes as opposed to their conversion to only grayscale images, the OC-SVM is applied with respect to four types of training data:

- With respect to the digital templates on:
 - the grayscale original codes \mathbf{x} ;
 - the RGB original codes \mathbf{x} .
- With respect to the physical references on:
 - the grayscale original codes \mathbf{x} ;
 - the RGB original codes \mathbf{x} .

To avoid the bias in the training data selection, the OC-SVM was trained five times on randomly chosen original printed samples \mathbf{x} and either digital templates or physical references. The OC-SVM was trained to minimize the P_{miss} on the validation sub-set. The obtained classification error is represented in Table IV. The visualisation of the OC-SVM decision boundaries is illustrated in Fig. 12.

Analyzing the obtained results, at first, it should be pointed out that the OC-SVM classification error based on the P_{miss} and P_{fa} is relatively high. At the same time, two important conclusions can be done:

- With respect to the chosen metrics the use of the digital templates is preferable than the printed references.
- Despite the visually grayscale nature of the CDP the authentication based on codes taken by the mobile phone in color mode is more efficient compared to the grayscale mode due to the fact that the different color channels have different sensitivity and due to the information loss while converting a three-channels color image into a single-channel grayscale one.

B. Deep processing domain data analysis

To further investigate the authentication performance, we consider an one-class classification based on the features extracted via DNN processing. In a particular case of the CDP authentication, where the reference templates \mathbf{t} are given, we consider a feature extractor based on a DNN auto-encoder

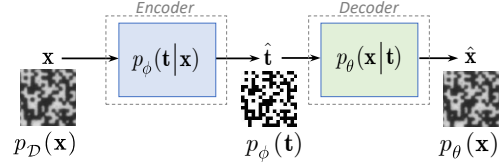


Fig. 13: General scheme of a deep model that aims at estimating the digital templates $\hat{\mathbf{t}}$ from the original printed codes \mathbf{x} with the following mapping of the estimated digital templates $\hat{\mathbf{t}}$ back to the printed codes $\hat{\mathbf{x}}$.

model $\mathbf{x} \rightarrow \hat{\mathbf{t}} \rightarrow \hat{\mathbf{x}}$, where $\hat{\mathbf{t}}$ is considered as a latent space representation as shown in Fig. 13. The difference with a generic auto-encoder consists in the fact that the latent space is represented by a space of digital templates in contrast to some generic low-dimensional representation in a generic auto-encoder.

The loss-function for the considered feature extracting system is defined as:

$$\mathcal{L}_{\text{One-class}}(\phi, \theta) = -I_{\phi}(\mathbf{X}; \mathbf{T}) - \beta I_{\phi, \theta}(\mathbf{T}; \mathbf{X}), \quad (6)$$

where β controls the relative importance of the two objectives.

The first mutual information term $I_{\phi}(\mathbf{X}; \mathbf{T})$ in (6) controls the mutual information between the estimate of template $\hat{\mathbf{t}}$ produced from \mathbf{x} based on the mapper $p_{\phi}(\mathbf{t}|\mathbf{x})$ and original template \mathbf{t} and is defined as:

$$\begin{aligned} I_{\phi}(\mathbf{X}; \mathbf{T}) &= \mathbb{E}_{p(\mathbf{x}, \mathbf{t})} \left[\log \frac{p(\mathbf{x}, \mathbf{t})}{p_{\mathcal{D}}(\mathbf{x})p_t(\mathbf{t})} \right] \\ &= \mathbb{E}_{p(\mathbf{x}, \mathbf{t})} \left[\log \frac{p_{\mathcal{D}}(\mathbf{x})p_{\phi}(\mathbf{t}|\mathbf{x})}{p_{\mathcal{D}}(\mathbf{x})p_t(\mathbf{t})} \right] \\ &= \mathbb{E}_{p(\mathbf{x}, \mathbf{t})} \left[\log \frac{p_{\phi}(\mathbf{t}|\mathbf{x})}{p_t(\mathbf{t})} \right]. \end{aligned} \quad (7)$$

According to [17], the variational decomposition is applied to decompose (7) into a form suitable for the practical calculations:

$$\begin{aligned} I_{\phi}(\mathbf{X}; \mathbf{T}) &= \mathbb{E}_{p(\mathbf{x}, \mathbf{t})} \left[\log \frac{p_{\phi}(\mathbf{t}|\mathbf{x})}{p_t(\mathbf{t})} \frac{p_{\phi}(\mathbf{t})}{p_{\phi}(\mathbf{t})} \right] \\ &= -\mathbb{E}_{p_t(\mathbf{t})} \left[\log \frac{p_t(\mathbf{t})}{p_{\phi}(\mathbf{t})} \right] - \mathbb{E}_{p_t(\mathbf{t})} [\log p_{\phi}(\mathbf{t})] \\ &\quad + \mathbb{E}_{p_{\mathcal{D}}(\mathbf{x})} [\mathbb{E}_{p_{\phi}(\mathbf{t}|\mathbf{x})} [\log p_{\phi}(\mathbf{t}|\mathbf{x})]], \end{aligned} \quad (8)$$

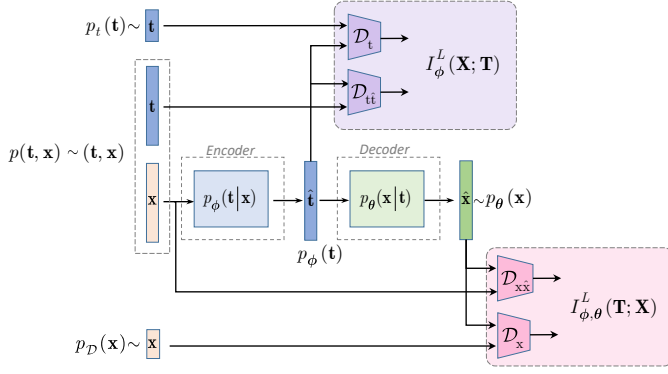


Fig. 14: The feature extraction for the one-class classification based on the estimation of the reference templates via D_{tt} and D_t and the printed codes via $D_{x\hat{x}}$ and D_x terms.

where $D_{\text{KL}}(p_t(\mathbf{t})\|p_\phi(\mathbf{t})) = \mathbb{E}_{p_t(\mathbf{t})} \left[\log \frac{p_t(\mathbf{t})}{p_\phi(\mathbf{t})} \right]$ is a Kullback–Leibler divergences between the true $p_t(\mathbf{t})$ and the posterior $p_\phi(\mathbf{t})$. $H(p_t(\mathbf{t}), p_\phi(\mathbf{t})) = -\mathbb{E}_{p_t(\mathbf{t})} [\log p_\phi(\mathbf{t})]$ is a cross-entropy.

Taking into account that the cross-entropy $H(p_t(\mathbf{t}), p_\phi(\mathbf{t})) \geq 0$, we get $I_\phi(\mathbf{X}; \mathbf{T}) \geq I_\phi^L(\mathbf{X}; \mathbf{T})$, where:

$$I_\phi^L(\mathbf{X}; \mathbf{T}) \triangleq \underbrace{\mathbb{E}_{p_D(\mathbf{x})} \left[\mathbb{E}_{p_\phi(\mathbf{t}|\mathbf{x})} [\log p_\phi(\mathbf{t}|\mathbf{x})] \right]}_{\mathcal{D}_{tt}} - \underbrace{D_{\text{KL}}(p_t(\mathbf{t})\|p_\phi(\mathbf{t}))}_{\mathcal{D}_t}. \quad (9)$$

The second mutual information term in (6) determined as $I_{\phi,\theta}(\mathbf{T}; \mathbf{X}) = \mathbb{E}_{p_D(\mathbf{x})} \left[\mathbb{E}_{p_\phi(\mathbf{t}|\mathbf{x})} \left[\log \frac{p_\theta(\mathbf{x}|\mathbf{t})}{p_D(\mathbf{x})} \right] \right]$ can be decomposed and bounded in a way similar to the first term: $I_{\phi,\theta}(\mathbf{T}; \mathbf{X}) \geq I_{\phi,\theta}^L(\mathbf{T}; \mathbf{X})$, where:

$$I_{\phi,\theta}^L(\mathbf{T}; \mathbf{X}) \triangleq \underbrace{\mathbb{E}_{p_D(\mathbf{x})} \left[\mathbb{E}_{p_\phi(\mathbf{t}|\mathbf{x})} [\log p_\theta(\mathbf{x}|\mathbf{t})] \right]}_{\mathcal{D}_{x\hat{x}}} - \underbrace{D_{\text{KL}}(p_D(\mathbf{x})\|p_\theta(\mathbf{x}))}_{\mathcal{D}_x}. \quad (10)$$

Remark: The term \mathcal{D}_t in (9) and the term \mathcal{D}_x in (10) can be implemented based on the density ratio estimation [18]. The terms \mathcal{D}_{tt} and $\mathcal{D}_{x\hat{x}}$ can be defined explicitly using Gaussian or Laplacian priors. In the Gaussian case, one can define $p_\phi(\mathbf{t}|\mathbf{x}) \propto \exp(-\lambda_1 \|\mathbf{t} - g_\phi(\mathbf{x})\|_2)$ and $p_\theta(\mathbf{x}|\mathbf{t}) \propto \exp(-\lambda_2 \|\mathbf{x} - f_\theta(\mathbf{t})\|_2)$ with the scale parameters λ_1 and λ_2 , which lead to ℓ_2 -norm, and $g_\phi(\mathbf{x})$ denotes the encoder and f_θ denotes the decoder. It also corresponds to the model $\mathbf{t} = g_\phi(\mathbf{x}) + \mathbf{e}_x$ and $\mathbf{x} = f_\theta(\mathbf{t}) + \mathbf{e}_t$, where \mathbf{e}_x and \mathbf{e}_t are the corresponding reconstruction error vectors following the Gaussian pdf.

Thus, the equation (9) reduces to:

$$I_\phi^L(\mathbf{X}; \mathbf{T}) = \underbrace{-\lambda_1 \mathbb{E}_{p_D(\mathbf{x})} \left[\mathbb{E}_{p_\phi(\mathbf{t}|\mathbf{x})} [\|\mathbf{t} - g_\phi(\mathbf{x})\|_2] \right]}_{\mathcal{D}_{tt}} - \underbrace{D_{\text{KL}}(p_t(\mathbf{t})\|p_\phi(\mathbf{t}))}_{\mathcal{D}_t}, \quad (11)$$

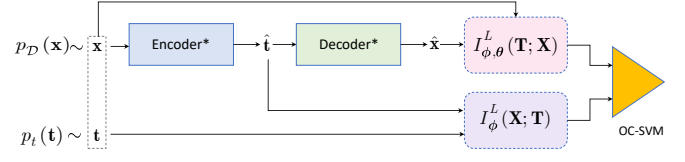


Fig. 15: The one-class classification training procedure: the encoder and decoder parts of the auto-encoder model shown in Fig. 14 are pre-trained and fixed (as indicated by a “*”); the OC-SVM is trained on the outputs of D_{tt} and D_t terms that are the results of $I_\phi^L(\mathbf{X}; \mathbf{T})$ decomposition and the $D_{x\hat{x}}$ and D_x terms that are the results of $I_{\phi,\theta}^L(\mathbf{T}; \mathbf{X})$ decomposition.

and (10) reduces to:

$$I_{\phi,\theta}^L(\mathbf{T}; \mathbf{X}) \triangleq \underbrace{-\lambda_2 \mathbb{E}_{p_D(\mathbf{x})} \left[\mathbb{E}_{p_\phi(\mathbf{t}|\mathbf{x})} [\|\mathbf{x} - f_\theta(\mathbf{t})\|_2] \right]}_{\mathcal{D}_{x\hat{x}}} - \underbrace{D_{\text{KL}}(p_D(\mathbf{x})\|p_\theta(\mathbf{x}))}_{\mathcal{D}_x}, \quad (12)$$

The final optimization problem schematically shown in Fig. 14 is:

$$\begin{aligned} (\hat{\phi}, \hat{\theta}) &= \underset{\phi, \theta}{\operatorname{argmin}} \mathcal{L}_{\text{One-class}}^L(\phi, \theta) \\ &= \underset{\phi, \theta}{\operatorname{argmin}} -(\mathcal{D}_{tt} - \mathcal{D}_t) - \beta(\mathcal{D}_{x\hat{x}} - \mathcal{D}_x). \end{aligned} \quad (13)$$

where:

$$\begin{aligned} \mathcal{D}_{tt} &\triangleq \mathbb{E}_{p_D(\mathbf{x})} \left[\mathbb{E}_{p_\phi(\mathbf{t}|\mathbf{x})} [\log p_\phi(\mathbf{t}|\mathbf{x})] \right], \\ \mathcal{D}_t &\triangleq D_{\text{KL}}(p_t(\mathbf{t})\|p_\phi(\mathbf{t})), \\ \mathcal{D}_{x\hat{x}} &\triangleq \mathbb{E}_{p_D(\mathbf{x})} \left[\mathbb{E}_{p_\phi(\mathbf{t}|\mathbf{x})} [\log p_\theta(\mathbf{x}|\mathbf{t})] \right], \\ \mathcal{D}_x &\triangleq D_{\text{KL}}(p_D(\mathbf{x})\|p_\theta(\mathbf{x})). \end{aligned} \quad (14)$$

In practice we considered four basic scenarios of features extractors for the one-class classification:

- 1) The reference templates estimation based on the term \mathcal{D}_{tt} :

$$\mathcal{L}_{\text{One-class}}^1(\phi, \theta) = -\mathcal{D}_{tt}. \quad (15)$$

- 2) The reference templates estimation based on the terms \mathcal{D}_{tt} and \mathcal{D}_t :

$$\mathcal{L}_{\text{One-class}}^2(\phi, \theta) = -\mathcal{D}_{tt} + \mathcal{D}_t. \quad (16)$$

- 3) The estimation of the reference templates and the printed codes based on terms \mathcal{D}_{tt} and $\mathcal{D}_{x\hat{x}}$:

$$\mathcal{L}_{\text{One-class}}^3(\phi, \theta) = -\mathcal{D}_{tt} - \beta \mathcal{D}_{x\hat{x}}. \quad (17)$$

- 4) The estimation of the reference templates and the printed codes based on terms \mathcal{D}_{tt} , \mathcal{D}_t , $\mathcal{D}_{x\hat{x}}$ and \mathcal{D}_x :

$$\mathcal{L}_{\text{One-class}}^4(\phi, \theta) = -\mathcal{D}_{tt} + \mathcal{D}_t - \beta \mathcal{D}_{x\hat{x}} + \beta \mathcal{D}_x. \quad (18)$$

In general case, to be comparable with the one-class classification in the spatial domain discussed in Section IV-A, the one-class classification model based on the OC-SVM is used.

The OC-SVM training procedure shown in Fig. 15 uses the pre-trained and fixed encoder and decoder parts of the auto-encoder model that serves as a features extractor. As an input

TABLE V: The OC-SVM classification error in deep processing domain (in %) ^a.

Model	Originals P_{miss}	Fakes #1 white P_{fa}	Fakes #1 gray P_{fa}	Fakes #2 white P_{fa}	Fakes #2 gray P_{fa}
<i>Based on the equation (19)</i>					
$\mathcal{L}_{\text{One-class}}^1 : -\mathcal{D}_{\hat{t}\hat{t}}$	0	6.38 (± 2.4)	8.23 (± 2.95)	0	0
$\mathcal{L}_{\text{One-class}}^2 : -\mathcal{D}_{\hat{t}\hat{t}} + \mathcal{D}_t$	0	6.81 (± 1.63)	7.09 (± 2.4)	0	0
$\mathcal{L}_{\text{One-class}}^3 : -\mathcal{D}_{\hat{t}\hat{t}} - \beta\mathcal{D}_{x\hat{x}}$	0	1.56 (± 0.32)	0.99 (± 0.81)	0	0
$\mathcal{L}_{\text{One-class}}^4 : -\mathcal{D}_{\hat{t}\hat{t}} + \mathcal{D}_t - \beta\mathcal{D}_{x\hat{x}} + \beta\mathcal{D}_x$	0	2.41 (± 1.38)	2.13 (± 1.59)	0	0
<i>Based on the equation (20)</i>					
$\mathcal{L}_{\text{One-class}}^3 : -\mathcal{D}_{\hat{t}\hat{t}} - \beta\mathcal{D}_{x\hat{x}}$	0	0.28 (± 0.64)	0	0	0
$\mathcal{L}_{\text{One-class}}^4 : -\mathcal{D}_{\hat{t}\hat{t}} + \mathcal{D}_t - \beta\mathcal{D}_{x\hat{x}} + \beta\mathcal{D}_x$	0.57 (± 1.27)	0	0.14 (± 0.32)	0	0
<i>Based on the OC-SVM</i>					
$\mathcal{L}_{\text{One-class}}^3 : -\mathcal{D}_{\hat{t}\hat{t}} - \beta\mathcal{D}_{x\hat{x}}$	0.28 (± 0.39)	0	0	0	0
$\mathcal{L}_{\text{One-class}}^4 : -\mathcal{D}_{\hat{t}\hat{t}} + \mathcal{D}_t - \beta\mathcal{D}_{x\hat{x}} + \beta\mathcal{D}_x$	0.14 (± 0.32)	0	0	0	0

^aThe python *OneClassSVM* method from the sklearn package is used with the following training parameters: kernel="rbf"; gamma=0.1; nu=0.0005.

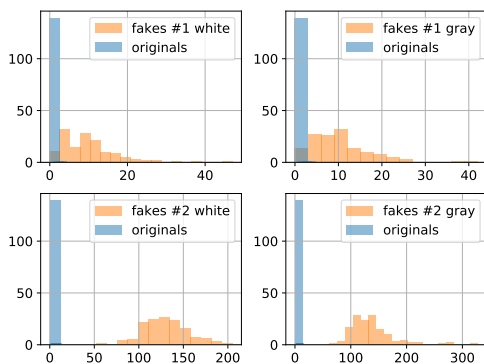


Fig. 16: The first scenario results' visualization: the histogram of symbol-wise Hamming distance (horizontal axis) between the original digital templates \mathbf{t} and the corresponding estimations $\hat{\mathbf{t}}$ obtained via the encoder model trained with respect to the term $\mathcal{D}_{\hat{t}\hat{t}}$.

the OC-SVM might take different combinations of outputs of four main terms: $\mathcal{D}_{\hat{t}\hat{t}}$, \mathcal{D}_t , $\mathcal{D}_{x\hat{x}}$ and \mathcal{D}_x . The exact scenarios are discussed in Sections IV-C1 - IV-C4 below.

C. Experimental results

1) *First scenario*: The optimization problem based on $\mathcal{L}_{\text{One-class}}^1(\phi, \theta) = -\mathcal{D}_{\hat{t}\hat{t}}$ aims at producing an accurate estimation $\hat{\mathbf{t}}$ of the corresponding binary digital template \mathbf{t} for each input printed original code \mathbf{x} . Taking into account that due to the nature of the used trained model the output estimation is real valued but not binary, at the inference stage, to measure the Hamming distance the final estimation $\hat{\mathbf{t}}$ is obtained by the thresholding with a threshold 0.5.

Fig. 16 illustrates the distributions of the symbol-wise Hamming distance between the original digital templates \mathbf{t} and the corresponding estimations $\hat{\mathbf{t}}$ obtained from the printed original and fake codes. Taking into account that the extracted feature vector consists only of one value, the OC-SVM is not

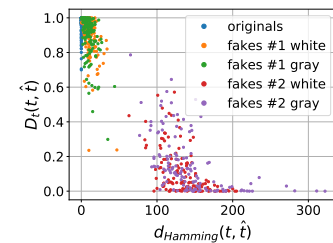


Fig. 17: The second scenario results' visualization: the 2D distribution of (i) the symbol-wise Hamming distance between the original digital templates \mathbf{t} and the corresponding estimations $\hat{\mathbf{t}}$ obtained via the encoder model trained with respect to the $\mathcal{D}_{\hat{t}\hat{t}}$ term and (ii) the corresponding responses of the discriminator model trained with respect to the \mathcal{D}_t term.

used and the classification is performed based on the decision rule:

$$\begin{cases} P_{fa} &= \Pr\{d_{\text{Hamming}}(\mathbf{t}, \hat{\mathbf{t}}) \leq \gamma_1 \mid \mathcal{H}_0\}, \\ P_{miss} &= \Pr\{d_{\text{Hamming}}(\mathbf{t}, \hat{\mathbf{t}}) > \gamma_1 \mid \mathcal{H}_1\}, \end{cases} \quad (19)$$

where P_{miss} is a probability of miss and P_{fa} is probability of false acceptance. The hypothesis \mathcal{H}_0 corresponds to the hypothesis that the input code is fake and the \mathcal{H}_1 corresponds to the hypothesis that the input code is original. Aiming to have $P_{miss} = 0$, the decision threshold γ_1 is determined on the validation sub-set to be equal to 2. The obtained classification error is given in Table V.

According to the obtained results, the one-class classification based on the encoder model trained with respect to the $\mathcal{D}_{\hat{t}\hat{t}}$ term as shown in Fig. 14 allows to distinguish the originals and the fakes #2 with 100% accuracy. The obtained P_{miss} and P_{fa} are confirmed by the distribution of the Hamming distance shown in Fig. 16. In case of the fakes #1, the corresponding distributions overlap and the P_{fa} is about 6 - 8%.

2) *Second scenario*: The optimization problem based on $\mathcal{L}_{\text{One-class}}^2(\phi, \theta) = -\mathcal{D}_{\hat{t}\hat{t}} + \mathcal{D}_t$ is an extension of the scenario IV-C1 with the discriminator part \mathcal{D}_t that aims to distinguish

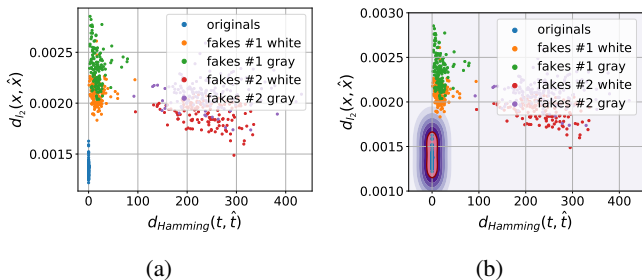


Fig. 18: The third scenario results' visualization: (a) the distribution of (i) the symbol-wise Hamming distance between the digital templates and its corresponding estimations via the encoder model trained with respect to the $\mathcal{D}_{\hat{t}\hat{t}}$ term and (ii) the ℓ_2 distance between the printed codes and its corresponding reconstructions by the decoder model trained with respect to the $\mathcal{D}_{x\hat{x}}$ term; (b) the OC-SVM decision boundaries.

between the distribution of original digital templates and its corresponding estimate.

Fig. 17 presents the 2D distribution of (i) the symbol-wise Hamming distance between the original digital templates \mathbf{t} and the corresponding estimations $\hat{\mathbf{t}}$ obtained based on the encoder model trained with respect to the $\mathcal{D}_{\hat{t}\hat{t}}$ term and (ii) the corresponding responses of the discriminator trained with respect to the \mathcal{D}_t term as shown in Fig. 14. It is easy to see that the obtained results are very close to those in Fig. 16 with respect to the Hamming distance, namely, the results for the original codes are close to zero and overlap with the fakes #1, while the fakes #2 are well separable. With respect to the \mathcal{D}_t discriminator decision the situation is similar, namely, the fakes #2 are well separable by the decision ratio smaller than 0.5 - 0.6. At the same time, for the the fakes #1 the decision ratio is bigger than 0.7 - 0.8 as well as for the originals.

The obtained authentication error based on the P_{miss} and P_{fa} calculated with respect to the decision rule (19) and given in Table V shows that the regularization via the discriminator \mathcal{D}_t does not have any significant influence and does not allow to improve the authentication accuracy.

3) *Third scenario:* In the third scenario $\mathcal{L}_{\text{One-class}}^3(\phi, \theta) = -\mathcal{D}_{\hat{t}\hat{t}} - \beta\mathcal{D}_{x\hat{x}}$ the term $\mathcal{D}_{x\hat{x}}$ is in charge of the printed codes reconstruction and plays a role of a learnable regularization.

Fig. 18a demonstrates the obtained distribution of two metrics: (i) the symbol-wise Hamming distance introduced in the Section IV-C1 and (ii) the ℓ_2 error between the printed codes and the corresponding reconstructions obtained as an output of the decoder model trained with respect to the $\mathcal{D}_{x\hat{x}}$ term as shown in Fig. 14 without any additional post-processing.

The obtained authentication results based on the decision rule (19) are given in Table V. It is easy to see that the learnable regularization via $\mathcal{D}_{x\hat{x}}$ term preserves the P_{miss} and P_{fa} on the fakes #2 to be zero, similar to the previous scenarios. At the same time, it allows to decrease the P_{fa} for the fakes #1 from 7% till 1-1.6%. Additionally, Table V presents the authentication results obtained based on the two

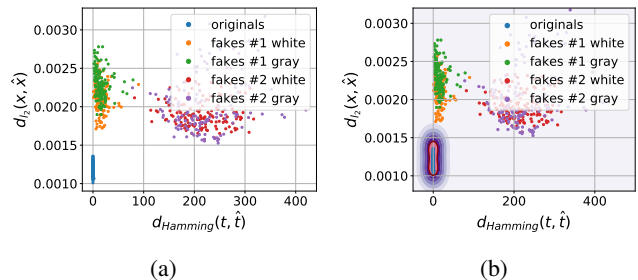


Fig. 19: The fourth scenario results' visualization: (a) the distribution of (i) the symbol-wise Hamming distance between the digital templates and its corresponding estimations via the encoder model trained with respect to the $\mathcal{D}_{\hat{t}\hat{t}}$ term and (ii) the ℓ_2 distance between the printed codes and its corresponding reconstructions by the decoder model trained with respect to the $\mathcal{D}_{x\hat{x}}$ term; (b) the OC-SVM decision boundaries.

metrics decision rule:

$$\begin{cases} P_{fa} &= \Pr\{d_{\text{Hamming}}(\mathbf{t}, \hat{\mathbf{t}}) \leq \gamma_1 \& \mathcal{D}_{\ell_2}(\mathbf{x}, \hat{\mathbf{x}}) \leq \gamma_2 \mid \mathcal{H}_0\} \\ P_{\text{miss}} &= \Pr\{d_{\text{Hamming}}(\mathbf{t}, \hat{\mathbf{t}}) > \gamma_1 \& \mathcal{D}_{\ell_2}(\mathbf{x}, \hat{\mathbf{x}}) > \gamma_2 \mid \mathcal{H}_1\}, \end{cases} \quad (20)$$

that allows to significantly reduce the P_{fa} for the fakes #1 to about 0.28%. Aiming to have the $P_{\text{miss}} = 0$, the decision constant γ_2 is determined on the validation sub-set to be equal 0.0017 and γ_1 equals to 2.

In addition, Table V includes the results of OC-SVM trained with respect to the metrics under investigation (the symbol-wise Hamming distance between the digital templates and its corresponding estimations via the encoder model trained with respect to the $\mathcal{D}_{\hat{t}\hat{t}}$ term and the ℓ_2 distance between the printed codes and its corresponding reconstructions by the decoder model trained with respect to the $\mathcal{D}_{x\hat{x}}$ term). The OC-SVM is trained only on the train sub-set of the original printed codes \mathbf{x} and its corresponding templates \mathbf{t} . The example of OC-SVM decision boundaries is illustrated in Fig. 18b. The OC-SVM reduces P_{fa} to 0% for all types of fakes. However, P_{miss} increases to about 0.28% in contrast to the previously obtained results with $P_{\text{miss}} = 0\%$.

4) *Fourth scenario:* The last considered scenario $\mathcal{L}_{\text{One-class}}^4(\phi, \theta) = -\mathcal{D}_{\hat{t}\hat{t}} + \mathcal{D}_t - \beta\mathcal{D}_{x\hat{x}} + \beta\mathcal{D}_x$ includes four terms: the main term $\mathcal{D}_{\hat{t}\hat{t}}$, the discriminator \mathcal{D}_t on the digital template estimation space, the printed code reconstruction space regularization $\mathcal{D}_{x\hat{x}}$ and the discriminator \mathcal{D}_x . Similarly to the third scenario, the OC-SVM is trained with respect to the two features: (i) the symbol-wise Hamming distance between the original digital templates and their estimations and (ii) the ℓ_2 distance between the printed codes and their reconstructions. A visual representation of the joint distribution of these metrics is shown in Fig. 19a. Table V includes the obtained one-class classification error based on three criteria: the decision rules (19) and (20) and the OC-SVM. The example of OC-SVM decision boundaries is illustrated in Fig. 19b.

TABLE VI: Execution time (hours) per 100 epochs on one NVIDIA GPU with a learning rate $1e-4$ for the considered scenarios.

Model	Execution time, hours
$\mathcal{L}_{\text{One-class}}^1 : -\mathcal{D}_{\text{tt}}$	2.78 - 3.05
$\mathcal{L}_{\text{One-class}}^2 : -\mathcal{D}_{\text{tt}} + \mathcal{D}_t$	5.12 - 5.25
$\mathcal{L}_{\text{One-class}}^3 : -\mathcal{D}_{\text{tt}} - \beta\mathcal{D}_{\text{x}\bar{x}}$	5.56 - 5.83
$\mathcal{L}_{\text{One-class}}^4 : -\mathcal{D}_{\text{tt}} + \mathcal{D}_t - \beta\mathcal{D}_{\text{x}\bar{x}} + \beta\mathcal{D}_x$	11.11 - 11.39

From the obtained results, one can note that in terms of decision rule (19), the regularization via \mathcal{D}_t and \mathcal{D}_x discriminators is counter-productive and makes the classification error bigger in comparison with the third scenario. In case of the decision rule (20), the regularization leads to a significant increase of P_{miss} . At the same time, the OC-SVM allows to decrease P_{miss} in two times, from 0.28% to 0.14% preserving P_{fa} equals to zero for all types of fakes.

In summary, it should be pointed out that despite the great performance of the fourth scenario's model its complexity is times higher compared with the other considered scenarios. The execution time complexity in hours per 100 training epochs is given in Table VI for each scenario.

V. CONCLUSION

In this work, we investigate the authentication aspects of modern CDP with respect to the typical hand-crafted copy fakes. To simulate the real-life conditions, we created the Indigo mobile dataset of CDP printed on the industrial printer and enrolled it via the mobile phone under regular light conditions.

The performed analysis of the base-line multi-class supervised classification of CDP reveals two important observations:

- In the general case, the model trained in a supervised way is capable to distinguish with a high accuracy the original CDP from the fakes produced on modern copy machines, which use built-in smart morphological processing enhancing image quality and reducing the dot gain for further reproduction.
- The quality of the fakes used for the training plays a very important role. The superior quality fakes closer to the original codes are of preference for the training and allow the model to authenticate the inferior quality fakes, even when the model does not see them during the training. In contrast, if the classifier is trained on the inferior quality fakes, then it is not capable to authenticate the superior quality fakes.

The performed analysis of CDP authentication based on the one-class classification shows that:

- In view of the great similarity between the original and fake codes the authentication in the spatial domain (i) is difficult with respect to the finding of right metrics and (ii) is not reliable enough due to the high overlapping between the classes.
- The authentication with respect to the digital templates is more efficient compared to the authentication with respect to the physical references.

- Despite the original black-and-white nature of the CDP the authentication based on codes taken by the mobile phone in color mode is more efficient compared to the grayscale mode.
- The authentication with respect to the DNN estimation of the digital templates and printed codes reconstruction is more efficient than the direct authentication with respect to the digital and printed codes in spatial domain.

The main disadvantage of the DNN based models is its high training complexity compared to the direct authentication in spatial domain. At the same time, at the inference stage, the trained models are equivalent in terms of authentication complexity to the authentication in spatial domain.

Besides the impressive performance of the one-class classification on real samples and mobile phone verification, it should be pointed out that the above analysis is done with respect to the typical HC copy attacks. In view of the widespread use of the ML technologies, the question about the robustness to the ML attacks is an important problem that we aim at investigating in our future work.

REFERENCES

- [1] J. Picard, "Digital authentication with copy-detection patterns," in *Optical Security and Counterfeit Deterrence Techniques V*, vol. 5310. International Society for Optics and Photonics, 2004, pp. 176–183.
- [2] J. Picard, P. Landry, and M. Bolay, "Counterfeit detection with qr codes," in *Proceedings of the 21st ACM Symposium on Document Engineering*, 2021, pp. 1–4.
- [3] R. Villán, S. Voloshynovskiy, O. Koval, and T. Pun, "Multilevel 2-d bar codes: Towards high-capacity storage modules for multimedia security and management," *IEEE Transactions on Information Forensics and Security*, vol. 1, no. 4, pp. 405–420, 2006.
- [4] I. Tkachenko, W. Puech, O. Strauss, C. Destruel, and J.-M. Gaudin, "Printed document authentication using two level or code," in *2016 IEEE International Conference on Acoustics, Speech and Signal Processing (ICASSP)*. IEEE, 2016, pp. 2149–2153.
- [5] H. P. Nguyen, A. Delahaies, F. Retraint, D. H. Nguyen, M. Pic, and F. Morain-Nicolier, "A watermarking technique to secure printed qr codes using a statistical test," in *2017 IEEE Global Conference on Signal and Information Processing (GlobalSIP)*. IEEE, 2017, pp. 288–292.
- [6] I. Tkachenko, W. Puech, C. Destruel, O. Strauss, J.-M. Gaudin, and C. Guichard, "Two-level qr code for private message sharing and document authentication," *IEEE Transactions on Information Forensics and Security*, vol. 11, no. 3, pp. 571–583, 2015.
- [7] R. Villán, S. Voloshynovskiy, O. Koval, and T. Pun, "Multilevel 2d bar codes: Towards high capacity storage modules for multimedia security and management," *IEEE Transactions on Information Forensics and Security*, vol. 1, no. 4, pp. 405–420, December 2006.
- [8] Y. Cheng, Z. Fu, B. Yu, and G. Shen, "A new two-level qr code with visual cryptography scheme," *Multimedia Tools and Applications*, vol. 77, no. 16, pp. 20 629–20 649, 2018.
- [9] A. E. Dirik and B. Haas, "Copy detection pattern-based document protection for variable media," *IET Image Processing*, vol. 6, no. 8, pp. 1102–1113, 2012.
- [10] O. Taran, S. Bonev, T. Holotyak, and S. Voloshynovskiy, "Adversarial detection of counterfeited printable graphical codes: towards "adversarial games" in physical world," in *IEEE International Conference on Acoustics, Speech and Signal Processing (ICASSP)*, 2020.
- [11] R. Yadav, I. Tkachenko, A. Trémeau, and T. Fournel, "Estimation of copy-sensitive codes using a neural approach," in *Proceedings of the ACM Workshop on Information Hiding and Multimedia Security*, 2019, pp. 77–82.
- [12] O. Taran, S. Bonev, and S. Voloshynovskiy, "Clonability of anti-counterfeiting printable graphical codes: a machine learning approach," in *IEEE International Conference on Acoustics, Speech and Signal Processing (ICASSP)*, Brighton, United Kingdom, May 2019.
- [13] *ISO/IEC 16022: Information technology - Automatic identification and data capture techniques - Data Matrix bar code symbology specification*, 2006.

- [14] G. Hinton and S. T. Roweis, "Stochastic neighbor embedding," in *NIPS*, vol. 15. Citeseer, 2002, pp. 833–840.
- [15] N. Otsu, "A threshold selection method from gray-level histograms," *IEEE transactions on systems, man, and cybernetics*, vol. 9, no. 1, pp. 62–66, 1979.
- [16] Y. Chen, X. S. Zhou, and T. S. Huang, "One-class svm for learning in image retrieval," in *Proceedings 2001 International Conference on Image Processing (Cat. No. 01CH37205)*, vol. 1. IEEE, 2001, pp. 34–37.
- [17] S. Voloshynovskiy, O. Taran, M. Kondah, T. Holotyak, and D. Rezende, "Variational information bottleneck for semi-supervised classification," in *Entropy Journal special issue "Information Bottleneck: Theory and Applications in Deep Learning"*, vol. 22, August 2020.
- [18] I. Goodfellow *et al.*, "Generative adversarial nets," *arXiv:1406.2661*, 2014.